HOKKAIDO UNIVERSITY

Title	Heat as a Tracer for Examining Depth-Decaying Permeability in Gravel Deposits
Author(s)	Sakata, Yoshitaka
Citation	Groundwater, 53(S1), 21-32 https://doi.org/10.1111/gwat.12236
Issue Date	2015-04
Doc URL	https://hdl.handle.net/2115/61038
Rights	This is the peer reviewed version of the following article: Groundwater, Volume 53, Issue S1, pages 21-32, April 2015, which has been published in final form at http://onlinelibrary.wiley.com/doi/10.1111/gwat.12236/abstract.
Type	journal article
File Information	Final manuscript for HUSCAP.pdf

Hokkaido University Collection of Scholarly and Academic Papers : HUSCAP

Heat as a tracer for examining depth-decaying permeability in gravel deposits

Yoshitaka Sakata

First affiliation: Division of Earth and Planetary Dynamics, Faculty of Science, Hokkaido University

North-10, West-8, Kita-ku, Sapporo, Hokkaido 060-0810, Japan

Second affiliation: Geotechnical Department, Division of Environmental Engineering, Docon Co., Ltd

1-5 Atsubetsu-chuo, Atsubetsu-ku, Sapporo, Hokkaido 004-8585, Japan

E-mail: yoshitaka_sakata@mail.sci.hokudai.ac.jp

Telephone/Fax: +81-11-801-1570

The author has no conflicts of interest to disclose.

Abstract

Depth dependence of permeability can appear in any geologic setting; however, vertical trends in alluvial gravel deposits are poorly understood because of the high variability of hydraulic conductivity K in monotonic sequences. This paper examines the sensitivity of depth-decaying permeability through heat transport simulation around a river's losing reach in the Toyohira River alluvial fan, Japan. Observed variations in groundwater temperature indicate that heat fluxes are dominant in the shallow zone, despite a vertical hydraulic gradient. In eight cases with different conditions (presence or absence of exponential decay trend, large or small variogram range, and cell isotropy or anisotropy) 1,000 K realizations are stochastically generated throughout a cross-sectional

model. The groundwater flow and heat transport are transiently calculated, and the averaged root mean square error $\overline{RMSE}$ is used for sensitivity comparison. The variance of $\overline{RMSE}$ shows that small $\overline{RMSE}$ realizations are effectively reproduced with vertical trend assumed. Plausible realizations of $\overline{RMSE}$ below a given threshold were obtained only when a vertical trend was assumed. The most plausible realization almost completely matched the observations. However, the number of plausible realizations per case was $\leq$10 and the median $\overline{RMSE}$ were insensitive to all the conditions. Statistical testing suggested that these plausible realizations may be statistically significant, aiding in generating a connected *K* zone for high heat flows. The cell anisotropy condition had the smallest effect on the simulation. Thus, effective modeling of the vertical trend contributes to heat transport; however, the model's efficiency is low without detailed information about the sedimentary structure.

Introduction

Depth-dependence of the permeability resulting from depositional and post-depositional processes may be found in any type of geologic formation. Geologic processes such as deltas, alluvial fans, and fluvial flows create unique patterns of hydrogeologic structure, not only in the

lateral direction but also vertically (Freeze and Cherry 1979). In alluvial fans, for example, increasing coarsening and fining with depth are typically seen as a result of progradation, retrogradation, and basin subsidence (Neton et al. 1994). On a smaller scale, streambeds may also exhibit vertical trends in grain size, probably related to hydraulic conductivity *K* (Marion et al. 2008; Chen 2011). Post-depositional processes also affect geological formation: compaction with buried depth, diagenesis, metamorphism, chemical cementation, and other processes (Domenico and Schwartz 1990; Ingebritsen et al. 2006). Such permeability decay with depth significantly affects groundwater flow systems not only on a regional scale (Saar and Manga 2004; Jiang et al. 2009), but also at multiple scales including hyporheic zones (Zlotnik et al. 2011). Permeability decay with depth was also discussed in relation to groundwater transport and residence time, as well as flow (Cardenas and Jiang 2010; Jiang et al. 2010a).

In a coarse sediment mixture, *K* is sensitive to changes in porosity, as shown in experimental studies (e.g., Koltermann and Gorelick 1995), laboratory tests (Major et al. 1997), and in-situ measurements (Yamaguchi and Nakamura 1994). However, the vertical trend of *K* has rarely been determined in alluvial gravel deposits. Multilevel in-situ measurements of *K* by pumping tests, slug

tests, flow meters and other means are expensive and susceptible to many sources of error such as skin effects (Butler et al. 1994). Even with many in-situ measurements, the trend would not be necessarily detected because of the strong heterogeneity of K on a smaller scale (e.g., Eggleston and Rojstaczer 1998). The sedimentary structure in alluvial gravel deposits consists of various components such as clast-supported gravel, matrix-supported gravel, and sand and finer materials (Rust 1979) and detailed information has only been obtained from a few outcrops and trenches (Jussel et al. 1994; Zappa et al. 2006). Even when detailed information is obtained, it is not valid to assume that the sedimentary texture of the upper layers extends to deeper layers. Generally, groundwater modeling of an unconsolidated gravel aquifer frequently assumes a constant value or homogeneity of K in the vertical direction.

The purpose of this study is to assess the effect of a decreasing trend of K on groundwater flow and transport in a numerical model of a typical monotonic gravelly aquifer. For this purpose, the author performed a sensitivity analysis of heat transport simulation around a losing river in the alluvial fan of the Toyohira River, Sapporo, Japan. Heat as a groundwater tracer is applicable in terms of robustness, convenience, and the low cost of field measurements (Anderson 2005).

Groundwater temperature can also be used as an alternative to measuring solute components, owing to the analogy of the governing equations in groundwater transport (Langevin et al. 2008). In particular, the thermal properties of rocks and fluids can be specified a priori or may be less sensitive to heat transport simulation than *K* (Anderson 2005), and thus temperature data can be used for estimating aquifer properties, especially as an inverse problem of *K* (e.g., Woodbury and Smith 1988; Wang et al. 1989; Bravo et al. 2002).

However, using groundwater temperature as a tracer is not necessarily an advantage relative to other tracers, especially for inferring a *K* pattern. Heat is transferred through the solid as well as the fluid, such that the thermal diffusivity of heat is several orders of magnitude larger than the molecular diffusion coefficient of other solute components (Domenico and Schwartz 1998). As a result, heat may be transformed mainly by conduction, including thermal diffusivity, and will be insensitive to convection, including groundwater velocity (i.e., *K*). In other words, measuring groundwater temperature would be effective in a situation of strong groundwater flow through relatively thick and permeable layers, for example, around a losing river in an alluvial fan. Several unique features such as the delay of the peak temperature arrival and the seasonal envelope are seen

in temperature variations at observation wells near a losing reach (Constantz 2008).

This study focuses on a shallow heat transport system in a recharge zone along the Toyohira River. Temperature observations show heat transport is dominated near the water table, indicating a vertical decrease of *K*. Here, a Monte Carlo approach is applied to simulate the anisotropic heat transport system. One thousand realizations of *K* were stochastically generated for eight study cases with a combination of the following three conditions (i.e., $2 \times 2 \times 2$): exponentially decreasing or constant vertical trend, large or small variogram of the residuals after detrending, and vertical isotropy or anisotropy at each cell. A coupled groundwater flow and heat transport model was constructed as a cross-sectional model of SEAWAT v.4. The average values of the root-mean-square residuals at the observation points were compared for the eight modeled cases. The sensitivity of the vertical trend and other heat transport simulation comparisons are discussed in terms of the probability of occurrence of the small error realizations.

Materials and methods

Study site

96 The field site is the Toyohira River alluvial fan in Sapporo, near 43°N, 141°E in Hokkaido,
97 the northernmost island of Japan (Figure 1). The city of Sapporo is the largest in northern Japan, and
98 with population currently over 1.9 million and increasing. The alluvial fan extends across ~35 km^2,
99 and is surrounded by Tertiary volcanic mountains to the west, hilly lands covered by Pleistocene
100 volcanic ash to the east, and lowland to the north. The fan comprises a western Holocene fan (gray
101 tone in Figure 1) 70–10 m above mean sea level (amsl) and an eastern Pleistocene fan (dark gray
102 tone) 90–20 m asl. The Toyohira River is about 72.5 km long with a watershed area of about 900
103 km^2. It flows south to north, almost through the center of the fan with an average inclination of about
104 7:1000, to the lowland around the Ishikari River (one of the main rivers in Japan). The median
105 values of the daily mean and drought discharges of this river in the fan were 12.6 and 4.0 m^3/s,
106 respectively, during the period 1974–2011. Synoptic discharge surveys (Sakata and Ikeda 2012)
107 revealed that the losing rate Q was about 1 m^3/s between kilometer point (KP) 15.5 and KP 17.0,
108 where KP is the distance units in kilometers along the river, as shown in Figure 1. Q was about 80%
109 of the total pumping rate of the city. The seepage rate per unit meter over distance q was about 2
110 $m^3/(m\ hr)$. Similar seepage values have been estimated for other losing reaches in Japan. This large

111 infiltration has been problematic for management of surface water use, especially during drought
112 periods.

113 Figure 1c shows the water table elevation contours (bold lines) and the vertical hydraulic
114 gradient contours (dashed lines) from a previous study (Sakata and Ikeda 2013a). The water table
115 gently declines northward in the downstream direction, with horizontal hydraulic gradients in the
116 order of magnitude of 10^{-2}. The water table rises along the river between KP 15 and 17; this section
117 includes the distinct losing section. On the other hand, the vertical hydraulic gradients are negative in
118 the fan area, that is, downward fluxes of groundwater are dominant there because of groundwater
119 withdrawals. The negative peak also extends to the river between KP 15.5 and 19.0, and the values
120 in the losing section (K.P. 15.5–17.0) are ranged between –0.1 and –0.2. The values are about one
121 order of magnitude larger than the horizontal gradients of the water table. The anisotropy of
122 hydraulic gradient also appears in the observation wells for this analysis, as described below.

123 Various Quaternary sediments such as gravel, sand, silt, clay, and humus underlie the middle
124 to distal parts of the Toyohira River alluvial fan. The hydrogeologic basement comprises Tertiary
125 volcanic formations in the upper fan from KP 18, and Pleistocene marine sediments in the middle

and distal fan. A subsurface gravel aquifer above the basement is divided into four sub-aquifers (Hu et al. 2010): Pleistocene Nos. IV and III, and Holocene Nos. II and I. The lowermost Pleistocene No. IV consists of alternating gravel, sand, and silt layers – the result of the transition of fluvial, delta, and shallow marine depositional systems. Both Pleistocene No. III and Holocene No. II aquifers consist mainly of alluvial fan gravel deposits, i.e., of poorly sorted andesite gravel with less than several percent fine content. The thickness of the gravel aquifer is over 100 m at the upper middle part of the Holocene fan, and less than 50 m at the distal part. Holocene No. I also consists of finer materials and appears only in the northern part of the fan (not in the study area).

Field observation

For the analysis data, the author conducted field observations of groundwater level and temperature in one deep well (DW-1) and three shallow wells (SW-1 to 3) along an off-stream transect at KP 16.6 (Figure 2). Distances from the center of the river channel are 76 m to DW-1, 80 m to SW-1, 140 m to SW-2, and 50 m to SW-3. The stratigraphic column at DW-1 shows a monotonic gravel sequence (i.e., Aquifers No. III and II) to a depth of about 63 m. A finer layer

141 appears at that depth, continuously lain with a gentle inclination to the east. The finer layer
142 corresponds to the top of Pleistocene aquifer IV, and serves as a hydrologic basement of gravel
143 deposits in the local area. Direct measurements of *K* by slug tests (solid squares at DW-1) might
144 show unobvious decrease of *K* with depth because of the large variation of *K* in the Holocene gravel
145 aquifer. Sakata and Ikeda (2013b) estimated the effective hydraulic conductivity $\overline{K}$ (open squares)
146 from the core properties. A moving average analysis (solid line) revealed a vertical trend from the
147 surface down to 30 m depth, and was established as an exponential function of depth *z* (m):

148 $$\overline{K} = \overline{K}_0 \exp(-Az) = 10^{-2.3} \exp(-0.11z) \qquad \text{at } z < z_0 \qquad (1)$$

149 where $\overline{K}_0$ is the average $\overline{K}$ value on the surface, from DW-1 and another borehole; *A* (m^{-1}) is a
150 decay exponent; and z_0 is the depth limit of the exponential decay (z_0 = 30 m in the fan). The depth
151 was also equal to the boundary between the Holocene No. II and Pleistocene III aquifers (Hu et al.
152 2010). This exponential model was used in previous studies (Saar and Manga 2004; Jiang et al.
153 2009; Zlotnik et al. 2011; Cardenas and Jiang 2010; Jiang et al. 2010a) and verified in a theoretical
154 study (Jiang et al. 2010b). However, the decay exponent in the fan was 10 to 1000 times that in
155 consolidated rocks, 1×10^{-2} to 1×10^{-4} m^{-1} (Jiang et al. 2009). The exponent decay reduced the

156 value of K at z = 30 m to only 1/25 of its value on the surface. Thus, the previous study suggests that
157 the large exponent decay may significantly affect the shallow systems of groundwater flow and
158 transport.

159 The groundwater level and temperature were automatically measured in each well using a
160 pressure transducer (HOBO U20 Water Level Data Logger U20-001-01; accuracy ±0.05%). At deep
161 well DW-1, the hydraulic head and temperature were observed at 15 m (DW-1-1), and the
162 groundwater temperature was also observed at two additional depths, 30 m (DW-1-2) and 60 m
163 (DW-1-3) using a thermal sensor (HOBO Water Temperature Pro v2 Data Logger U22-001;
164 accuracy ±0.2°C). The screen interval of DW-1 was 1 m between 63 and 64 m depth, and those of
165 the shallow wells SW-1, SW-2, and SW-3 were a few meters below the water table. The set of deep
166 well DW-1 and shallow well SW-1 (2 m apart) formed a piezometer nest. Observations were
167 conducted from 10 June 2010 to 28 February 2011 (264 days). The river stage was observed at the
168 upper gauging station of KP 17.8, and the data were converted to those measured at KP 16.6 using a
169 linear relationship (R^2 = 0.96). All the original data were acquired hourly, but daily average data were
170 used in the analysis to smooth uncertain fluctuations, including measurement errors.

171 Figure 3 shows the observed water level and temperatures of the groundwater and surface
172 water. The water table levels in the shallow wells were usually lower than the river stage, but among
173 them they varied almost in parallel. Sudden rises caused by precipitation were rarely seen during the
174 observation period, indicating that the groundwater recharge depends mainly on surface water
175 infiltration within the local area. The water table levels at SW-1 and SW-2 were nearly identical, and
176 the water table at SW-3 was lower than at other shallow wells, although SW-3 was closer to the
177 river channel. Thus, the average horizontal hydraulic gradients (dimensionless) from the river were
178 substantially different, 0.007 at SW-1, 0.004 at SW-2, and 0.018 at SW-3. The hydraulic head at
179 DW-1 was about 7–8 m lower than the water table at SW-1; the average vertical hydraulic gradient
180 was –0.11, indicating a downward flow. The magnitude was about one order larger than that of the
181 horizontal hydraulic gradient, as shown in Figure 1c. The water-level variation at DW-1 was
182 relatively smooth, and the seasonal fluctuation probably reflected the water cycle (e.g., reduced
183 recharge in winter) and the intake of the city (e.g., pumping for cooling in summer).

184 The surface water temperature varied daily and seasonally, reaching a low of 1.0°C on 18
185 December and a high of 20.6°C on 6 September (Figure 3b). In the well nearest the river, SW-3, the

groundwater temperature almost matched the smoothed temperature of the surface water, probably indicating preferential flows east of the river. The groundwater temperature at SW-1 and SW-2 showed smoother fluctuations and delayed peaks (13.4°C on 28 October at SW-1 and 12.0°C on 2 December at SW-2). At the deep well DW-1, the groundwater temperatures fluctuated in a much narrower range than at the shallow wells, and the temperature at DW-1-3 at 60 m depth was constant at 10.3°C, indicating an isothermal layer near the bottom, despite the large hydraulic gradient in the downward direction. In other words, the shallow heat transfer might be affected by permeability, in terms of Darcy's law.

Heat transport model

A simulation of the coupled groundwater flow and heat transport was performed on a cross section similar to that of the observation transect. The SEAWAT v.4 simulation program (Thorne et al. 2006; Langevin et al. 2008) in Visual MODFLOW 2009.1 (Schlumberger) was used in this study. Figure 4 illustrates the grid design and boundary conditions. The total length between SW-2 (left; west) and SW-3 (right; east) was 190 m (lateral coordinate $x = -140$ m to 50 m), and the total depths

varied between 54 m on the eastern side and 64 on the western side. The vertical grid spacing was 1 m, except for the lowermost layer. The horizontal grid spacing was also 1 m between the river channel and SW-1 (x = 80 m), and 5 m on the east and west sides. Anderson and Woessner (1992) recommended that the increase in cell widths in such finite-difference models should be no more than 1.5 times the original width. However, in this study the grid was designed so that the stochastic realizations of K per 1-m regular grid were smoothly input into the numerical model. The inflow condition was set for the upper cells of the river channel (x = −15 m to 5 m) using the "River Boundary" function of MODFLOW. The river stage and temperature were variable in time as shown in Figure 3a (black line), and K of the streambed was assumed to be 1×10^{-2} m/s, which was sufficient to allow for water infiltration. The outflow boundaries on both sides were represented using the "Drainage Boundary" condition of MODFLOW rather than the "Constant Head Boundary." This was because the constant head boundary compels unrealistic downward flows from the groundwater table to the bottom. The drainage elevations varied daily, and were linearly interpolated from the water table to the west of SW-2 or the east of SW-3 vertically downward according to the vertical hydraulic gradient between SW-1 and DW-1. No vertical flows and heat

fluxes were assumed for the other upper cells based on the assumption that the seepage loss was the dominant recharge source within the local area. No flow and fluxes were also assumed for the bottom cells based on the assumption that the permeability of the bottom fine layer was negligible. The seasonal temperature profiles at DW-1 commonly showed that the temperature gradient was only about 0.3 °C /100m at the bottom depth (Sakata 2013). The initial conditions of the hydraulic head and temperature were estimated from maps drawn manually from observation data at the start date, 10 June 2010.

Stochastic realization of hydraulic conductivity

This study generated stochastic realizations of K following the modeling concept of a vertical trend on a scale of tens of meters, and small-scale heterogeneity on a 1-m scale. One simple way to apply this is to detect a trend, simulate the residuals, and then return to the trend (Nowak and Verly 2004). The logarithmic conductivity Y [log (m/s)] was used instead of K, because K was assumed to be log-normal (Domenico and Schwartz 1998; ASCE 2008). $Y(\boldsymbol{s})$ at any location $\boldsymbol{s}$ (x, z) in the cross section is formulated as a sum of the trend component $M(z)$ and residual component $R(\boldsymbol{s})$:

231 $$Y(\boldsymbol{s}) = \log K(\boldsymbol{s}) = M(z) + R(\boldsymbol{s}) \qquad (2)$$

232 $M(z)$ was assumed a function only of the depth z (m), and independent of distance x (m). $M(z)$ was

233 assumed a common logarithm of Equation (1), in which $\overline{K}_0$ was replaced by $10^{-3.07}$ as the value at

234 the location of DW-1. $M(z)$ was also assumed to be constant below the limited depth z_0 as:

235 $$M(z) = -3.07 - 0.047z \quad \text{at } z < 30 \text{ m} \qquad (3a)$$

236 $$M(z) = -4.50 \quad \text{at } z \geq 30 \text{ m} \qquad (3b)$$

237 The equation also assumes heterogeneity with a vertical trend in Holocene aquifer no. II and

238 stationary heterogeneity in Pleistocene aquifer no. III. This study assumed $R(\boldsymbol{s})$ as a regional

239 variable with the same variogram throughout the analysis domain, as detailed geologic information

240 for dividing the monotonic sequence was not obtained. Sequential Gaussian simulation (SGS) was

241 used for its stochastic realization as in other sandy gravel aquifer modeling (Eggleston et al. 1996;

242 Jang and Liu 2004; Lee et al. 2007). The SGS process has six steps (Deutsch and Journel 1998): 1)

243 input the honor data (solid squares in Figure 2), which are equal to the estimates at the nodes. 2)

244 Generate a random path though the grid nodes. 3) Select the first node in that path and estimate a

245 mean and standard deviation at that node by normal or ordinary kriging based on the surrounding

honor data. 4) Obtain a random value from the mean and standard deviation and set the value at the node. 5) Include the newly simulated value as part of the honor data. 6) Repeat steps 2 to 5 until all the grid nodes have simulated values. The SGS in this study was performed using a free Fortran code *sgsim* in GSLIB (Deutsch and Journel 1998).

The realizations by SGS are significantly dependent on the variogram model. The variogram of $R(\boldsymbol{s})$ in the fan was previously formulated by Sakata (2013) who used 134 slug-test results and performed variogram analysis using original data of $R(\boldsymbol{s})$ and obtained a histogram that was approximately Gaussian at 95% significance level. Consequently, a spherical anisotropic model of distance h was obtained as:

$$\gamma(h) = c + b\left[\frac{3}{2}\frac{h}{a} - \frac{1}{2}\left(\frac{h}{a}\right)^3\right] \qquad (4)$$

In Sakata (2013), the sill b and nugget c were determined to be nearly identical in the horizontal and vertical directions (b = 1.0 and c = 0.5). The range a differed in the x and z directions, a_x = 1000 m in the lateral direction and a_z = 20 m in the vertical. Such large range anisotropy was also observed in nature (Deutsch 2007). However, the estimated ranges may be too large on the local scale used in this analysis compared with other field studies (e.g., Hess et al. 1992; Rubin 2003). Gelhar (1993)

261 summarized the correlation scales of horizontal and vertical K on an overall scale less than 1 km.
262 The relationship indicated that a correlation scale of 100 m was probably 10 to 20 m in the
263 horizontal direction, and a few meters in the vertical direction (Figure 6.6 in the text of Gelhar).
264 Thus, the author examined the residual variogram on two different scales, large (a_x = 1000 m and a_z
265 = 20 m) and small (a_x = 10 m and a_z = 2 m), in addition to the presence or absence of a vertical
266 decreasing trend. The sill and nugget parameters were probably also different among the local and
267 basin scales as well as the ranges. However, the values in the previous analysis were consistently
268 used in this study because only eight Y honor data were obtained in the cross section. The sill and
269 nugget values generated a relatively random field of K and the value of K changed by several orders
270 of magnitude between adjacent points. The variance of the Y honor data was 1.2, which was nearly
271 equal to the sum of the nugget and sill.

272 One thousand realizations of the residuals were generated on the 1-m regular grid
273 throughout the cross-section for the two variogram ranges (large and small). Next, the logarithmic
274 conductivity $Y(\boldsymbol{s})$ was obtained by adding the simulated residuals to the trend component (Equation
275 (3)). For this process, another constant trend M_0 was also assumed instead of the vertical trend. M_0

276 was simply calculated at –4.17, as an integral average of Equation (3) from the surface to the bottom
277 of the aquifer at DW-1. Figure 5 shows extracted examples of the residuals (panels a and b) and the
278 resulting logarithm of K (panels c to f). Panel c shows the most plausible realization from a total of
279 8000, as described below. The residuals were generated using the large (panel a) and small (panel b)
280 variogram ranges, respectively. Both realizations demonstrate variability in about four orders of
281 magnitude among the 1-m regular grids. These images also include slightly decreasing trends with
282 depth as a result of the conditional simulation with the honor data at DW-1. The simulation that used
283 the large-range condition (panel a) produced relatively continuous zones of high K value (red and
284 orange) and low K value (light and dark blue). On the other hand, the small range condition (panel
285 b) shows almost randomly patched zones, probably typical alluvial gravel deposits. The images of Y
286 (panels c and e) were obtained by adding the vertical trend to panels a and b, resulting in relatively
287 high and low Y values in the shallow and deep layers. The lower images (panels d and f) were
288 obtained by adding a constant mean to the same residuals, producing mostly vertical trends that are
289 masked in the large heterogeneity.

290 The stochastic realizations of $Y(\boldsymbol{s})$ were inversely log-transformed to $K(\boldsymbol{s})$, which was assigned

291 to each cell in the numerical model. $Y(\boldsymbol{s})$ in the lowermost layer and on both sides of the 5-m-wide
292 cells was obtained by averaging all the $Y(\boldsymbol{s})$ values of the 1-m grid cells. In the final modeling step,
293 the ratio of vertical/horizontal anisotropy was also considered for assessing further small-scale
294 heterogeneity within a depth of 1 m (Freeze and Cherry 1979; Burger and Belitz 1997). The
295 vertical/horizontal anisotropy ratio R varies in space; therefore, individual values should be given at
296 each cell. However, the author prepared two simplified cases in which all the cells had a constant
297 isotropic ratio (R =1) or were assigned an anisotropy value (R = 0.1). Other aquifer and fluid
298 properties were assumed to be constant in this simulation. The total porosity was 0.2 and the specific
299 storage was set to 10^{-5} m^{-1}. The heat capacities and densities of the andesitic gravel deposits were
300 850 J/kg/°C and 2600 kg/m^3, and those of the fluid were 4183 and 1000, respectively. The thermal
301 conductivities of the bulk and fluid were 2.5 and 0.6 W/m/°C, respectively. The longitudinal and
302 transverse thermal diffusivity values were 10 and 0.1. These thermal parameters were less sensitive
303 to the heat transport simulation than K (Sakata 2013). The dependencies of the fluid density and
304 viscosity on temperature were assigned from the literature (Voss 1984; Langevin et al. 2008).
305

306 **Error estimation**

307 The coupled groundwater flow and heat transport simulation was run in transient mode from
308 10 June 2010 through 28 February 2011 (264 days) with 24 time steps (hourly). The calculated
309 temperature was extracted each day at six observation points, i.e., at three depths of DW-1 (index j =
310 1, 2, 3) and at the three shallow wells, SW-1 (j = 4), SW-2 (j = 5), and SW-3 (j = 6). The model
311 fitting in each realization was assessed by least squares; the fit between simulated values and field
312 measurements was quantified using squared differences. The individual root mean square error
313 $\overline{RMSE}_j$ values were calculated at each observation point (j = 1 to 6), and the average root mean
314 square error $\overline{RMSE}$ was then obtained from the six values of the individual $\overline{RMSE}_j$:

315 $$\overline{RMSE} = \frac{1}{N_w}\sum_{1}^{N_w} RMSE_j \qquad (5a)$$

316 $$RMSE_j = \sqrt{\frac{1}{N_d}\sum_{i=1}^{N_d}\left(T_j(t_i) - T_j^*(t_i)\right)^2} \qquad (5b)$$

317 where N_w is the number of observation points for assessing the fit (6 here). N_d is the number of
318 transient calculation outputs (264). $T^*(t_i)$ and $T(t_i)$ are the calculated and observed temperatures at
319 each calculation time t_i (i = 1 to 264 day), respectively. The statistical values of the average $\overline{RMSE}$
320 were summarized, and the cumulative percentage curves of $\overline{RMSE}$ plotted for comparison. In this

321 study, the criterion of $\overline{RMSE}$ for a good match between the model and observations was defined as
322 1.0 °C. The average range of the groundwater fluctuations is 6.52 °C; therefore, the normalized error
323 of the criterion is about 15 % (1.0/6.52). The author believes that obtaining an error range within
324 about 10–20 % is probably difficult in groundwater transport simulation. Indeed, the error estimator
325 $\overline{RMSE}$ was affected not only by the comparison conditions but also by various factors such as
326 measurement errors, uncertainty in initial and boundary conditions, and model restrictions in the
327 cross section. Here, the criterion is considered to be suitable because it revealed a statistical
328 discrepancy of $\overline{RMSE}$ among the eight study cases, and the calculated temperature time-series
329 visually match those of the observations, as shown below. Consequently, the realizations of $\overline{RMSE}$
330 that were less than the criterion value were extracted as “plausible.”
331

332 # Results

333 ## Error Statistics

334 For each of the eight cases, Table 1 summarizes the statistical values of the $\overline{RMSE}$, median
335 (*Me*), variance (*Var*), minimum value (*Min*), and the number of $\overline{RMSE}$ realizations less than 1°C (*N*

336 $\overline{RMSE}$) for 1000 realizations. Figure 6 shows the cumulative percentage curves of $\overline{RMSE}$ for each case.

337 *Me* was in a narrow range between 2.5°C and 2.9°C, and was insensitive to any of the model

338 conditions. This means that most of the realizations failed to calculate the high heat flow around the

339 losing river. This was because $\overline{RMSE}$ was calculated at 2.92°C in the special case where the

340 temperatures in all the cells did not vary from the initial condition. The actual average seepage rate

341 from the river boundary was about 0.2 m^3/(m hr), and the value was only one tenth of the observed

342 seepage rate q (2 m^3/(m hr)). The root mean square errors of the groundwater head in the realizations

343 were over about 1 m in the deep and shallow wells. The failures in most realizations were probably

344 due to the limitation of Gaussian simulation in this study. Gaussian simulation cannot reproduce

345 extremely high values of simulated variables (Koltermann and Gorelick 1996; Lee et al. 2007).

346 However, the exchange of heat between the surface water and groundwater is dependent on such

347 preferential flow paths such as buried channels (e.g., Woessner 2000). Moreover, in this study, the Y

348 honor data were limited to only one borehole and detailed geologic information around the losing

349 river. This Monte Carlo approach using a total of eight thousands realizations indicated that the heat

350 transport simulation may be inefficient unless the typical conduits of high heat flows are identified in

advance, at least to an approximate extent.

Despite the low efficiency of the method, small $\overline{RMSE}$ values were frequently obtained as *Var* increased since *Me* was nearly equal in all the study cases. In Figure 6, when *Var* increased, the cumulative percentage curves of $\overline{RMSE}$ had relatively gentle slopes. The cases that had a vertical trend (red lines) had a more gentle slope than those without the trend (blue lines). The large variogram range (bold lines) also tended to produce a leftward shift in the area compared with the cases with a small range (thin lines), although the change appears smaller than that associated with the presence or absence of a vertical trend. The condition of cell anisotropy appears to have a smaller effect than the other two conditions. The relation of *Min* among the eight cases was opposite to that of *Var*; *Min* in the vertical trend cases was consistently smaller than in the constant trend cases, independent of the other conditions. *Min* in the large range cases was also smaller than in the small range cases, as well as in the vertical trend cases. However, the relation of *Min* with regard to cell-isotropy and anisotropy was not obvious. Especially in the large range cases, *Min* of the cell-isotropy cases was nearly equal to that of the anisotropy case.

$N_{\overline{RMSE}}$ is another probability index that indicates how often plausible realizations were

366 generated. As shown in Table 1, the largest $N_{\overline{RMSE}}$ was 10 in Case 2. The second largest was 4 in

367 Case 1. The smallest number was 2 in Case 3. These cases were common in terms of the

368 exponentially decaying pattern of *K*. No plausible realizations were achieved in the other study

369 cases. This also indicates that modeling the exponentially decreasing trend may be essential for

370 obtaining plausible realizations. However, no plausible realization was achieved in Case 4, which

371 also contained a vertical trend as did Cases 1 through 3. Moreover, where plausible cases were

372 found, their occurrence corresponds to a probability of ≤ 1% of the 1000 realizations. Thus, one

373 might argue that $N_{\overline{RMSE}}$ in the latter three cases may not be as statistically significant as the other

374 cases ($N_{\overline{RMSE}} = 0$). To verify this, a statistical test was performed on the hypothesis that $N_{\overline{RMSE}}$ was

375 obtained rarely (less than or equal to 1%) but randomly, that is, independent of the vertical trend,

376 variogram range, and cell anisotropy (i.e., the Poisson distribution). The probability P_0 of no

377 occurrence ($N_{\overline{RMSE}} = 0$) among *n* trials was simply calculated with the mean probability *p*: $P_0 = (1-$

378 $p)^n$. For the statistical hypothesis, the mean probability of the occurrence of $\overline{RMSE} < 1$°C in 1000

379 samples was assumed to be $p_1 = 0.002$ ($N_{\overline{RMSE}} = 2$ in Case 3), $p_2 = 0.004$ ($N_{\overline{RMSE}} = 4$ in Case 1), and p_3

380 $= 0.01$ ($N_{\overline{RMSE}} = 10$ in Case 2). Thus, the probabilities of $N_{\overline{RMSE}} = 0$ were 0.14, 0.02, and <0.01,

respectively. For $N_{\overline{RMSE}} = 2$ in Case 3, the hypothesis was accepted with a significance level of 95%. This indicates that Case 3 with a vertical trend, small variogram range, and cell anisotropy conditions may not be different in terms of reproducing plausible realizations from other cases of $N_{\overline{RMSE}} = 0$. On the other hand, the hypothesis was rejected for $N_{\overline{RMSE}} = 4$ in Case 1 and $N_{\overline{RMSE}} = 10$ in Case 2. Thus, it can be concluded that the plausible realizations of $\overline{RMSE} < 1$°C were statistically significant in Cases 1 and 2, i.e., those with a combination of the vertical trend and large variogram range, relative to the other cases.

Temperature time series

Figure 7 shows the calculated temperature time-series for the smallest $\overline{RMSE}$, i.e., *Min*, realizations in each study case. At the deepest point DW-1-3, all the results were nearly identical with the observation of a constant temperature of 10.1°C. This indicates that the isothermal layer was independent of the spatial variability of *K*, and was realized based on the boundary conditions. For the shallow SW-3 well, all the calculations also achieved almost satisfactory matching with observations. The average $\overline{RMSE}$ values were obtained for individual $\overline{RMSE}_j$ of six points, but the

averaging was most affected by $\overline{RMSE}_6$ at SW-3 because $\overline{RMSE}_6$ varied the most among the different realizations, with relation to large fluctuations of groundwater temperature as a result of high heat flows.

The temperatures observed in the shallow wells SW-1 and SW-2 showed typically smooth fluctuations with different peak delays. All the results of Cases 1 to 5 calculated the typical delay at a relatively close shallow well, SW-1. In Cases 6 and 7 the peak delay was longer while in Case 8 the calculated temperature at SW-1 was almost constant, indicating no heat fluxes in the west direction. At SW-2, however, the peak delay was in good agreement with the observations in Cases 1, 2, and 3. The results were equal to those in which the plausible realizations were obtained ($N_{\overline{RMSE}} > 0$). On the other hand, in Cases 4 to 8, almost no fluctuation indicated that most of the heat fluxes infiltrated into the deeper layer, due to downward flows.

Finally, Cases 1, 2, and 3 were compared at the deep well DW-1-1 and DW-1-2. Case 1 showed little fluctuations compared with the observation at DW-1-2 while in Case 3, very little fluctuations were calculated at DW-1-1. Only the realization in Case 2 provided some fluctuations at both DW-1-2 and DW-1-1 as a result of heat flow toward these points. Therefore, the realization in

411 Case 2, as previously shown in Figure 5c, may be the most plausible among the 8000 realizations.
412 The average seepage rate in the realization was 2 m^3/(m hr), which was equal to the observed rate *q*.
413 The RMSE of the hydraulic head was only 0.12 m in SW-1 and 0.6 m in DW-1. These values are
414 within the accepted values of anisotropic heat transfer around the losing river. Note that the
415 calculated temperatures at DW-1-2 were not well matched because the heat fluxes from the previous
416 winter occurred within the calculation period.
417

418 ## Discussion

419 This study used heat as a groundwater tracer for examining depth-decaying permeability in a
420 monotonic gravel aquifer, in the Toyohira River alluvial fan. Around the losing river reach,
421 groundwater temperature was applied as a tracer for the sensitivity analysis of *K*. Heat transport
422 simulation was performed using stochastic realizations of *K*. Another unique aspect of this study was
423 the simulation of the spatial variability of *K* using a combination of multiple-scale heterogeneity: the
424 exponential decreasing trend with depth on a scale of tens of meters, the stochastic residuals between
425 1-m regular grids, and cell anisotropy within a depth of 1 m. One thousand realizations of the

426 residuals were generated by SGS and converted to Y by adding the trend component. Back log-
427 transformed K were input to the SEAWAT model in eight comparison cases with different
428 conditions: the presence or absence of vertical trend, large or small variogram range, and cell-
429 isotropy or anisotropy. The average $\overline{RMSE}$ at six observation points was used for comparison with
430 the observations, and the statistical parameters were compared.

431 The variance of the $\overline{RMSE}$ indicates that the cases with the vertical trend condition had smaller
432 $\overline{RMSE}$ values. Plausible realizations of $N_{\overline{RMSE}}$ were obtained only in the cases that simulated a vertical
433 trend. When the vertical trend was assumed, the plausible realizations were obtained in cases of
434 either large or small ranges, and cell isotropy or anisotropy. The relative sensitivity is noteworthy,
435 because the change of K by vertical trend (one to two orders of magnitude) was smaller than the
436 random variation by SGS (four orders of magnitude). In this study, several realizations with the
437 smallest $\overline{RMSE}$ values provide a good match with observations when the vertical trend is included.
438 The most plausible model showed an almost perfect match to the observations in terms of
439 groundwater temperature, hydraulic head, and seepage rate. Therefore, modeling the exponential
440 decrease may be an important factor in the description of the shallow heat transport, and of other

441 solute components such as artificial contaminants infiltrated from the surface.

442 In this study, however, the effect of modeling the vertical trend was not pronounced because
443 the number of plausible realizations $N_{\overline{RMSE}}$ was only ten or less, i.e., 1% of 1000 realizations. The
444 mean $\overline{RMSE}$ was insensitive to the introduced conditions and nearly equal to the value for the case
445 when the groundwater temperature is assumed to remain steady at its initial level. These results also
446 provided much lower seepage rates from the river boundary, compared with the observations. In
447 particular, a statistical test suggested that $N_{\overline{RMSE}}$ may be significant only when the vertical trend and
448 large range conditions are present. The large range condition was particularly helpful for SGS in
449 reproducing a high-*K* connected area as a conduit. Thus, the vertical trend was probably essential to
450 the anisotropic heat transport system; however, a sedimentary structure that included preferential
451 flow paths is also required for a high heat flow system around the losing river. In this study, the
452 preferential flow paths were specified among thousands of realizations with a (maybe unrealistic)
453 large range condition. This approach was too inefficient, and the simulations were validated using a
454 limited number of observation data (only six points in this study). Additional information about
455 zones of increased groundwater flow may be combined with the stochastic modeling to improve the

456 efficiency of obtaining plausible realizations. For example, a delineation of the hydrofacies,
457 including preferential flow paths (e.g., open-framework gravel) can be obtained near the surface.
458 The shallow information is then interpolated to the deeper layers, based on data from a number of
459 high-quality cores, a high-resolution geophysical survey (e.g., Regli et al. 2002; Bennett et al. 2006)
460 and other advanced methods such as hydraulic tomography (Berg and Illman 2011). In future work,
461 indicator simulation or other advanced methods could provide good realizations of complex
462 heterogeneity, as shown in several innovative studies (Weissmann et al. 1999; Felletti et al. 2006;
463 Ramanathan et al. 2010; Guin et al. 2010). These field and numerical methods are probably
464 applicable but practically limited, as suggested in this paper. Another approach based on calibration
465 such as the parameter estimation method PEST may be effective when field data are limited.

466 The vertical/horizontal ratio of the anisotropy of K at each 1-m cell helps prevent downward
467 groundwater flow, as well as the vertical decreasing trend on a scale of tens of meters. This study
468 also showed that the $N_{\overline{RMSE}}$ in Case 2 with anisotropy was more than double the $N_{\overline{RMSE}}$ in Case 1 with
469 isotropy. The most plausible realization included the anisotropic condition; however, the statistical
470 test suggested that the effect of the cell anisotropy condition was not larger than that of the other two

471 comparison conditions. The heterogeneity within 1 m was probably insensitive to the shallow heat
472 transport on this scale. In this study, the vertical/horizontal anisotropy was assumed to be constant
473 throughout the area even though the value actually varies in space. Modeling the cell anisotropy will
474 also be required in future work.

475 Finally, several other uncertainties and limitations in the present analysis are discussed. First,
476 the exponential decay trend (Equation (1)) is probably unique to this alluvial fan. Other gravelly
477 aquifers may show different magnitudes of decay exponent, other functions (e.g., a simple linear
478 trend), or unobvious trends with a small exponent. In this heat transport simulation, similar
479 conclusions may be derived using a linear trend fitted to the exponential model in the shallow depth.
480 The vertical change of K must be established individually at each site using multi-level in-situ tests,
481 core-analysis, and other methods. Additionally, the number of observation points (six points in this
482 study) was probably not sufficient for inferring the complex heterogeneity in the gravel deposits. To
483 improve the reliability of the results, several shallow wells should be installed between SW-1 and
484 SW-2, and at least one deep well in addition to DW-1. The error criterion should be changed to a
485 more reasonable one, considering several other factors of error. Finally, restricting the model within

the cross section may affect the small number of plausible realizations, because the generated K patterns act as if the domain was extended infinitely in the y plane. 3D modeling would be required for more rigorous treatment, although its computational cost may be a limiting factor.

Conclusions

In this study heat was used as a groundwater tracer to analyze the modeling of the vertical decrease of K in monotonic gravel sequences of the Toyohira River alluvial fan. The observations indicated a dominant heat flux in the shallow zone, despite a vertical hydraulic gradient, implying a hydrogeologic structure, including a vertical decrease. Heat transport simulation was performed using stochastic realizations of K, based on the Monte Carlo approach. One thousand realizations of K were reproduced using a combination of the exponentially decreasing trend and small-scale heterogeneity generated by SGS. Eight different conditions were modeled: the presence or absence of a vertical trend, large or small variogram range, and cell isotropy or anisotropy. The averaged root mean square error $\overline{RMSE}$ at six observation points was calculated for each realization, and the statistical values were compared.

501 The mean of $\overline{RMSE}$, *Me,* was insensitive to the eight modeled conditions, and in many
502 realizations the seepage rate from the river boundary was much smaller than in the observations.
503 This means that the SGS did not generate reliable preferential flow paths for high heat flow with the
504 limited honor data available. Despite its inefficiency, plausible realizations with $\overline{RMSE}$ below the
505 threshold (the criterion temperature of 1°C) were obtained when the vertical trend condition was
506 present, although the systematic change of *K* with depth was two orders of magnitude smaller than
507 the small-scale heterogeneity. Several realizations with vertical trend agreed with the observations,
508 and the most plausible one was almost a complete match in terms of groundwater temperature,
509 hydraulic head, and seepage rate. This indicates that the vertical trend effectively contributed to the
510 anisotropic heat transport system.

511 However, there were fewer than ten plausible realizations among the 1000 realizations,
512 including those with the vertical decrease. A statistical test suggests that the plausible realizations
513 with the vertical trend and large variogram range conditions may be statistically significant. The
514 variogram range condition was probably unrealistic, but aided in generating a high-connected zone.
515 The cell-anisotropy condition also increased the plausibility of the realizations, but the effect was

slight compared with that of the other conditions. In conclusion, the modeling in this study showed that the vertical trend was essential in the anisotropic heat transport; however, for describing high heat transport, detailed information of the smaller-scale heterogeneity, including preferential flow paths, is required to produce statistically significant results.

Acknowledgements

The author sincerely thanks Prof. Ryuji Ikeda of Hokkaido University for the meaningful discussions, suggestions, and comments, and would like to acknowledge the Hokkaido Regional Development Bureau for the use of the observation wells. This study greatly benefited from the assistance of Sayuri Watanabe, Yoko Yamamoto, Hideki Otake, and Akinari Honda, who provided technical support and prepared the numerous datasets. The comments of two anonymous reviewers, the associate Editor, and Dr. F Schwartz, Chief Editor of this journal, led to substantial improvements of this manuscript.

References

Anderson, M.P., and W.W., Woessner. 1992. *Applied Groundwater Modeling Simulation of Flow and Advective Transport*. London: Academic Press.

Anderson, M.P. 2005. Heat as a ground water tracer. *Ground Water* 43, no. 6: 951–968. DOI:10.1111/j.1745-6584.2005.00052.x

ASCE (American Society of Civil Engineers). 2008. *Standard guideline for fitting saturated hydraulic conductivity using probability density function*. ASCE/EWRI 50–08. Reston, Virginia: ASCE.

Bennett, V,G.L., G.S., Weissmann, G.S, Baker, and D.W., Hyndman. 2006. Regional-scale assessment of a sequence-bounding paleosol on fluvial fans using ground-penetrating radar, eastern San Joaquin Valley, California. *Bulletin of the Geological Society of America* 118: 724–732.

Berg, S.J., and W.A., Illman. 2011. Three-dimensional transient hydraulic tomography in a highly heterogeneous glaciofluvial aquifer-aquitard system. *Water Resources Research* 47, no. 10, W10507. DOI:10.1029/2011WR010616

545 Bravo, H.R., F., Jiang, and R.J., Hunt. 2002. Using groundwater temperature data to constrain
546 parameter estimation in a groundwater flow model of a wetland system. *Water Resources*
547 *Research* 38, no. 8: 28–1–28–14. DOI:10.1029/2000WR000172
548 Burger, R.L., and K., Belitz. 1997. Measurement of anisotropic hydraulic conductivity in
549 unconsolidated sands: A case study from a shoreface deposit, Oyster, Virginia. *Water Resources*
550 *Research* 33, no. 6: 1515–1522. DOI:10.1029/97WR00570
551 Butler, Jr., J.J., G.C., Bohling, Z., Hyder, and C.D., McElwee. 1994. The use of slug tests to describe
552 vertical variations in hydraulic conductivity. *Journal of Hydrology* 156: 137–162. DOI:
553 10.1016/0022-1694(94)90075-2
554 Cardenas, M.B., and X.-W., Jiang. 2010. Groundwater flow, transport, and residence times through
555 topography-driven basins with exponentially decreasing permeability and porosity. *Water*
556 *Resources Research* 46, no. 10. DOI:10.1029/2010WR009370
557 Chen, X. 2011. Depth-dependent hydraulic conductivity distribution patterns of a streambed.
558 *Hydrological Processes* 25, no.2: 278–287. DOI:10.1002/hyp.7844
559 Constantz, J. 2008. Heat as a tracer to determine streambed water exchanges. *Water Resources*

560 *Research* 44, no. 4, W00D10. DOI:10.1029/2008WR006996

561 Deutsch, C.V., and A.G., Journel. 1998. *GSLIB Geostatistical Software Library and User's Guide*

562 2nd ed. New York: Oxford University Press.

563 Deutsch, C.V. 2007. A review of geostatistical approaches to data fusion. In *Subsurface Hydrology*:

564 *Data Integration for Properties and Processes*, ed. D.W., Hyndman, F.D., Day–Lewis, and K.,

565 Singha, 7–18. Geophysical Monograph 171. Washington, D.C.: AGU. DOI:10.1029/171GM03

566 Domenico, P.A., and F.W., Schwartz. 1998. *Physical and Chemical Hydrogeology* 2nd ed. New

567 York: Wiley.

568 Eggleston, J.R., S.A., Rojstaczer, and J.J., Peirce. 1996. Identification of hydraulic conductivity

569 structure in sand and gravel aquifers: Cape Cod data set. *Water Resources Research* 32, no. 5:

570 1209–1222. DOI:10.1029/96WR00272

571 Eggleston, J.R., and S., Rojstaczer. 1998. Identification of large-scale hydraulic conductivity trends

572 and influence of trends on contaminant transport. *Water Resources Research* 34, no. 9: 2155–

573 2168. DOI:10.1029/98WR01475

574 Felletti, F., R., Bersezio, and M., Giudici. 2006. Geostatistical simulation and numerical upscaling, to

575 model ground-water flow in a sandy-gravel, braided river, aquifer analogue. *Journal of*
576 *Sedimentary Research* 76, no. 11: 1215–1229. DOI:10.2110/jsr.2006.091

577 Freeze, R.A., and J.A., Cherry. 1979. *Groundwater*. Englewood Cliffs, New Jersey: Prentice-Hall.

578 Gelhar, L.W. 1993. *Stochastic Subsurface hydrology*. Englewood Cliffs, New Jersey: Prentice Hall.

579 Guin, A., R., Ramanathan, R.W., Ritzi, Jr., D.F., Dominic, I.A., Lunt, T.D., Scheibe, and V.L.,
580 Freedman. 2010. Simulating the heterogeneity in braided channel belt deposits: 2. Examples of
581 results and comparison to natural deposits. *Water Resources Research* 46, no. 4, W04516.
582 DOI:10.1029/2009WR008112

583 Hess, K.M., S.H., Wolf, and M.A., Celia. 1992. Large-scale natural gradient tracer test in sand and
584 gravel, Cape Cod, Massachusetts: 3. Hydraulic conductivity variability and calculated
585 macrodispersivities. *Water Resources Research* 28, no. 8: 2011–2027.
586 DOI:10.1029/92WR00668

587 Hu, S.G., S., Miyajima, D., Nagaoka, K., Koizumi, and K., Mukai. 2010. Study on the relation
588 between groundwater and surface water in Toyohira-gawa alluvial fan, Hokkaido, Japan. In
589 *Groundwater Response to Changing Climate*, ed. M., Taniguchi, and I.P., Holman, 141–157. AK

590 Leiden, Netherlands: CRC Press. DOI:10.1201/b10530–13

591 Ingebritsen, S.E., W.E., Sanford, and C.E., Neuzil. 2006. *Groundwater in Geologic Processes*, 2nd

592 ed. Cambridge: Cambridge University Press.

593 Jang, C.S., and C.W., Liu. 2004. Geostatistical analysis and conditional simulation for estimating the

594 spatial variability of hydraulic conductivity in the Choushui River alluvial fan, Taiwan.

595 *Hydrological Processes* 18, no. 7: 1333–1350. DOI:10.1002/hyp.1397

596 Jiang, X.W., L., Wan, X.S., Wang, S., Ge, and J., Liu. 2009. Effect of exponential decay in hydraulic

597 conductivity with depth on regional groundwater flow. *Geophysical Research Letters* 36, no. 24.

598 DOI:10.1029/2009GL041251

599 Jiang, X.W., X.S., Wang, and L., Wan. 2010a. Semi-empirical equations for the systematic decrease

600 in permeability with depth in porous and fractured media. *Hydrogeology Journal* 18, no. 4: 839–

601 850. DOI:10.1007/s10040-010-0575-3

602 Jiang, X.W., L., Wan., M.B., Cardenas, S. Ge, and X.S., Wang. 2010b. Simultaneous rejuvenation

603 and aging of groundwater in basins due to depth decaying hydraulic conductivity and porosity.

604 *Geophysical Research Letters* 37, no. 5, L05403. DOI:10.1029/2010GL042387

605 Jussel, P., F., Stauffer, and T., Dracos. 1994. Transport modeling in heterogeneous aquifers: 1.
606 Statistical description and numerical generation of gravel deposits. *Water Resources Research*
607 30, no. 6: 1803–1817. DOI:10.1029/94WR00162
608 Koltermann, C.E., and S.M., Gorelick. 1995. Fractional packing model for hydraulic conductivity
609 derived from sediment mixtures. *Water Resources Research* 31, no. 12: 3283–3298.
610 DOI:10.1029/95WR02020
611 Koltermann, C.E., and S.M., Gorelick. 1996. Heterogeneity in sedimentary deposits: a review of
612 structure-imitating, process-imitating, and descriptive approaches. *Water Resources Research* 32,
613 no. 9: 2617–2658. DOI:10.1029/96WR00025
614 Langevin, C.D., D.T., Thorne, Jr., A.M., Dausman, M.C., Sukop, and W., Guo. 2008. *SEAWAT*
615 *Version 4: A computer program for simulation of multi species solute and heat transport*.
616 Techniques and Methods 6, A22. Reston, Virginia: USGS.
617 Lee, S.Y., S.F., Carle, and G.E., Fogg. 2007. Geologic heterogeneity and a comparison of two
618 geostatistical models: Sequential Gaussian and transition probability-based geostatistical
619 simulation. *Advances in Water Resources* 30, no. 9: 1914–1932.

620 DOI:10.1016/j.advwatres.2007.03.005

621 Major, J.J., R.M., Iverson, D.F., McTigue, S., Macias, and B.K., Fiedorowicz. 1997. Geotechnical
622 properties of debris-flow sediments and slurries, In *Debris flow Hazards Mitigation: Mechanics,*
623 *Prediction, and Assessment*, ASCE Proceedings of First International Conference, ed. C.L.
624 Chen, 249–259. San Francisco: ASCE.

625 Marion, A., A.I., Packman, M., Zaramella, and A. Bottacin-Busolin. 2008. Hyporheic flows in
626 stratified beds. *Water Resources Research* 44, no. 9. DOI:10.1029/2007WR006079

627 Neton, M.J., J., Dorsch, C.D., Olson, and S.C., Young. 1994. Architecture and directional scales of
628 heterogeneity in alluvial-fan aquifers. *Journal of Sedimentary Research* 64, no. 2b : 245–257.
629 DOI:10.1306/D4267FA0-2B26-11D7-8648000102C1865D

630 Nowak, M. and G., Verly. 2004. The practice of sequential Gaussian simulation. In *Geostatistics*
631 *Banff*, Ed., O., Leuangthong, and C.V., Deutsch, 387–398. Netherlands, Dordrecht: Springer.
632 DOI:10.1007/978–1–4020–3610–1_39

633 Ramanathan, R., A. Guin, R.W., Ritzi, Jr., D.F., Dominic, V.L., Freedman, T.D., Scheibe, and I.A.,
634 Lunt. 2010. Simulating the heterogeneity in braided channel belt deposits: 1. A geometric-based

635 methodology and code. *Water Resources Research* 46, no. 4. DOI:10.1029/2009WR008111

636 Regli, C., P., Huggenbergera, P., and M., Rauberb. 2002. Interpretation of drill core and georadar
637 data of coarse gravel deposits. *Journal of Hydrology* 255 no. 1–4: 234–252. DOI:
638 10.1016/S0022-1694(01)00531-5

639 Rubin, Y. 2003. *Applied stochastic hydrogeology*. New York: Oxford university press.

640 Rust, B.R. 1979. Facies Models 2. Coarse Alluvial Deposits. In *Facies Models*, ed. R.G., Walker,
641 11–21. Toronto: Geological Association of Canada.

642 Saar, M.O., and M., Manga. 2004. Depth dependence of permeability in the Oregon Cascades
643 inferred from hydrogeologic, thermal, seismic, and magmatic modeling constraints. *Journal of*
644 *Geophysical Research* 109: B04204. DOI:10.1029/2003JB002855

645 Sakata, Y., and R., Ikeda. 2012. Quantification of longitudinal river discharge and leakage in an
646 alluvial Fan by synoptic survey using handheld ADV. *Journal of Japan Society of Hydrology*
647 *and Water Resources* 25, no. 2: 89–102 (in Japanese).

648 Sakata, Y., and R., Ikeda. 2013a. Regional mapping of vertical hydraulic gradient using uncertain
649 well data: a case study of the Toyohira River alluvial fan, Japan. *Journal of Water Resource and*

650 *Protection* 5, no. 8: 823–834. DOI:10.4236/jwarp.2013.58083

651 Sakata, Y., and R., Ikeda. 2013b. Depth dependence and exponential models of permeability in
652 alluvial-fan gravel deposits. *Hydrogeology Journal* 21, no. 4: 773–786. DOI:10.1007/s10040-
653 013-0961-8

654 Sakata, Y. 2013. 5 Stochastic simulation of groundwater-flow and heat-transport. In *Geostatistical*
655 *reservoir modeling of trending heterogeneity specified in focused recharge zone: a case study of*
656 *Toyohira River alluvial fan, Sapporo, Japan*, 112–149. Ph.D. dissertation, Hokkaido University,
657 Sapporo, Japan.

658 Thorne, D., C.D., Langevin, and M.C., Sukop. 2006. Addition of simultaneous heat and solute
659 transport and variable fluid viscosity to SEAWAT. *Computer and Geosciences* 32: 1758–1768.
660 DOI:10.1016/j.cageo.2006.04.005

661 Voss, C.L. 1984. *A finite-element simulation model for saturated-unsaturated, fluid-density-*
662 *dependent ground-water flow with energy transport or chemically-reactive single-species solute*
663 *transport*, Water-Resources Investigations Report 84–4369. Reston, Virginia: USGS.

664 Wang, K., P.Y., Shen, and A.E., Beck. 1989. A solution to the inverse problem of coupled

665 hydrological and thermal regimes. In *Hydrogeological Regimes and Their Subsurface Thermal*
666 *Effects*, ed. A.E. Beck, G. Garven, and L. Stegena, Geophysical Monograph Series 47. no. 2: 7–
667 21. Washington, D.C.: American Geophysical Union.
668 Weissmann, G.S., S.F., Carle, and G.E., Fogg. 1999. Three-dimensional hydrofacies modeling based
669 on soil survey analysis and transition probability geostatistics. *Water Resources Research* 35, no.
670 6: 1761–1770. DOI:10.1029/1999WR900048
671 Woessner, W.W. 2000. Stream and fluvial plain ground water interactions: rescaling hydrogeologic
672 thought. *Ground Water*, 38 No. 3: 423–429, DOI:10.1111/j.1745-6584.2000.tb00228.x
673 Woodbury, A.D., and L., Smith. 1988. Simultaneous inversion of hydrogeologic and thermal data: 2.
674 Incorporation of thermal data. *Water Resources Research* 24, no. 3: 356–372.
675 DOI:10.1029/WR024i003p00356
676 Yamaguchi, Y., and A., Nakamura. 1994. Change of permeability of shallow foundation for fill dams
677 due to excavation and embankment. *Journal of Groundwater Hydrology* 36, no. 4: 423–438 (in
678 Japanese).
679 Zappa, G., R., Bersezio, F., Felletti, and M., Giudici. 2006. Modeling heterogeneity of gravel-sand,

680 braided stream, alluvial aquifers at the facies scale. *Journal of Hydrology* 325, no. 1–4: 134–153.

681 DOI:10.1016/j.jhydrol.2005.10.016

682 Zlotnik, V.A., M.B. Cardenas, and D. Toundykov. 2011. Effects of multiscale anisotropy on basin

683 and hyporheic groundwater flow. *Ground Water*, 49 No. 4: 576–583, DOI: 10.1111/j.1745-

684 6584.2010.00775.x

685

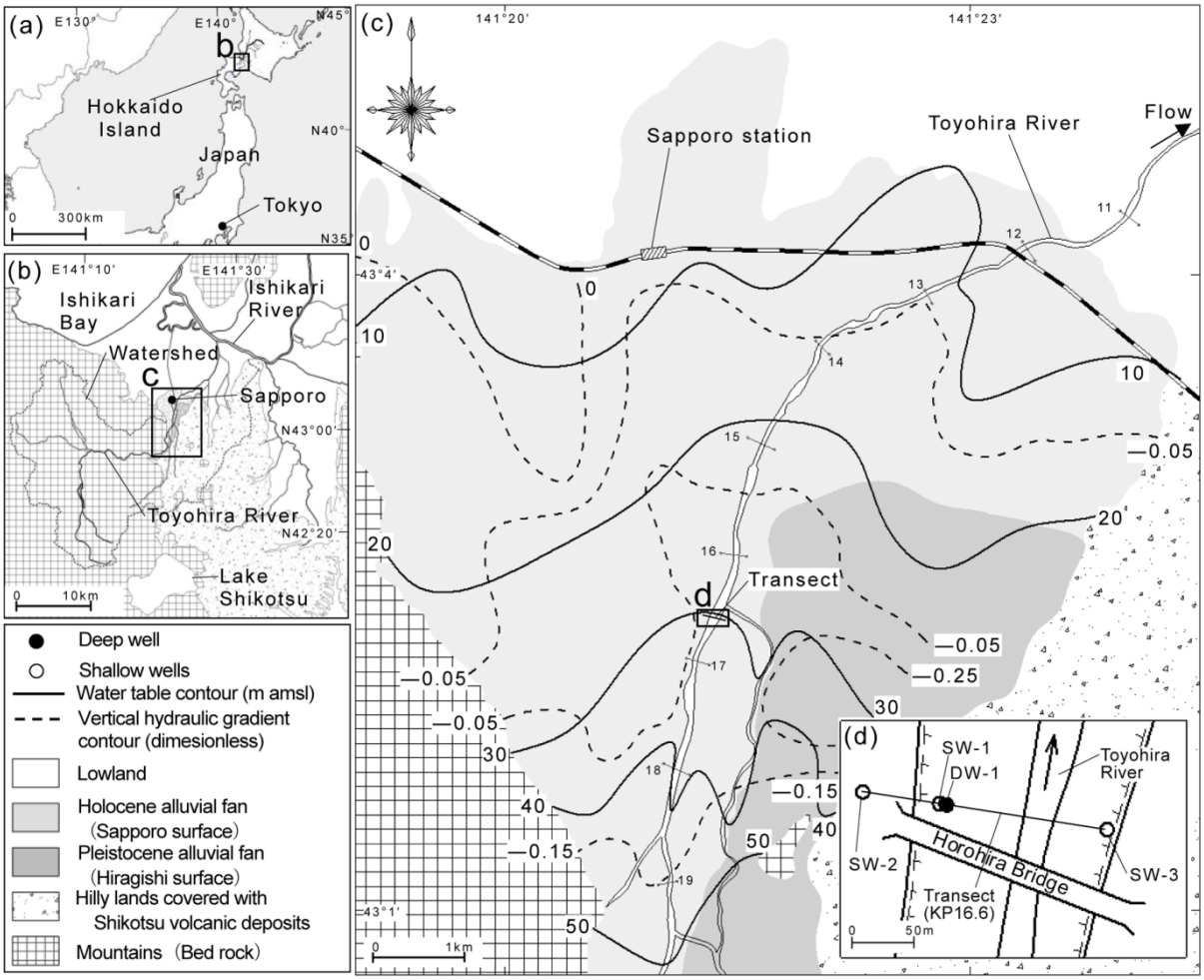

686

687 Figure 1 Location maps and topographic features of study area of Toyohira River alluvial fan.

688

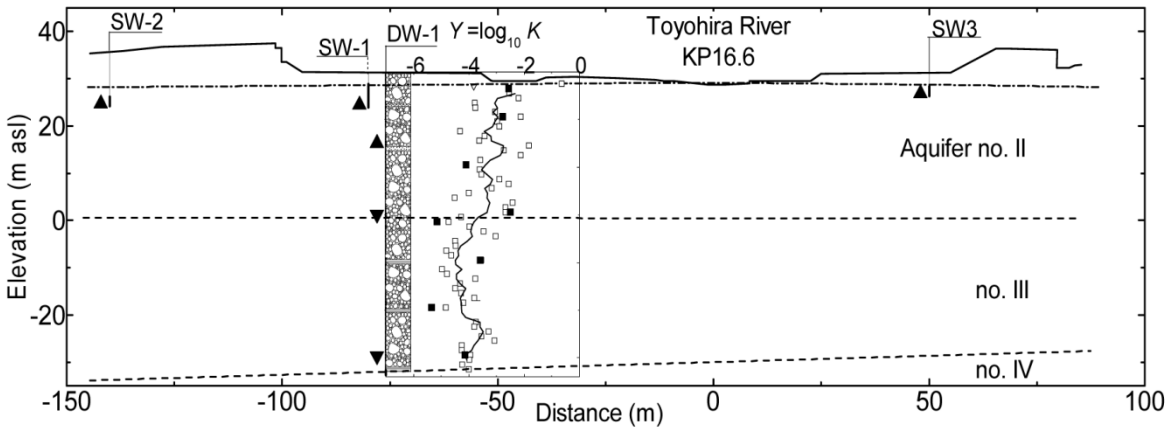

Figure 2 Cross section of the study area showing observation locations. Solid triangles represent water pressure and temperature observations, and inverted triangles are those of temperature alone. Aquifers II, III, and IV are described in the text. The vertical profile of *Y* was taken from Sakata and Ikeda (2013b); solid squares, open squares, and solid line denote *Y* values measured by slug tests, *Y* values estimated from undisturbed cores, and moving averages of estimated *Y*, respectively.

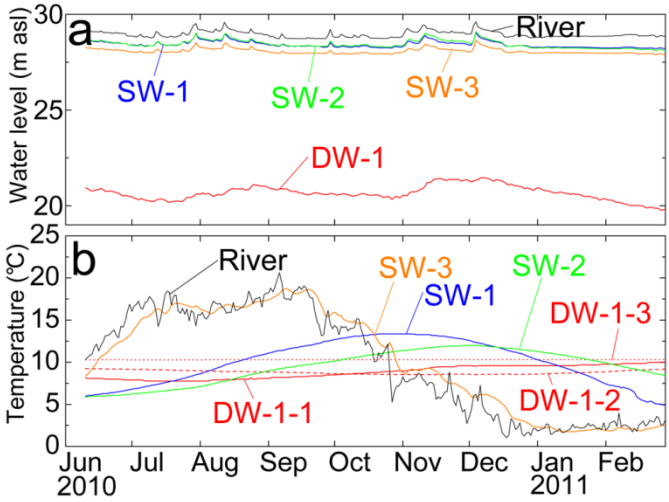

Figure 3 Daily mean variations of water level (a) and temperature (b) in the river and observation wells.

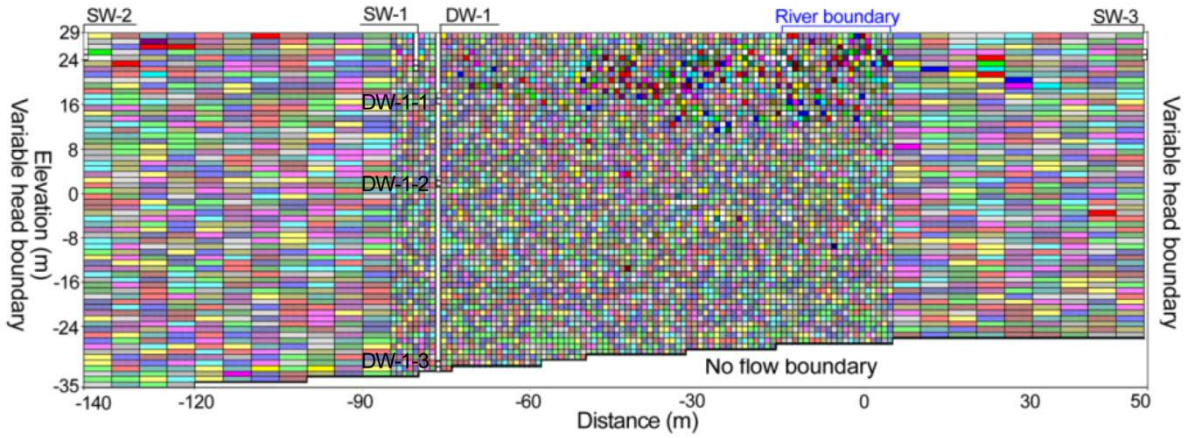

699

700 Figure 4 Cross-sectional simulation model of SEAWAT. The random color of each cell was assigned

701 from the realization of *K*.

702

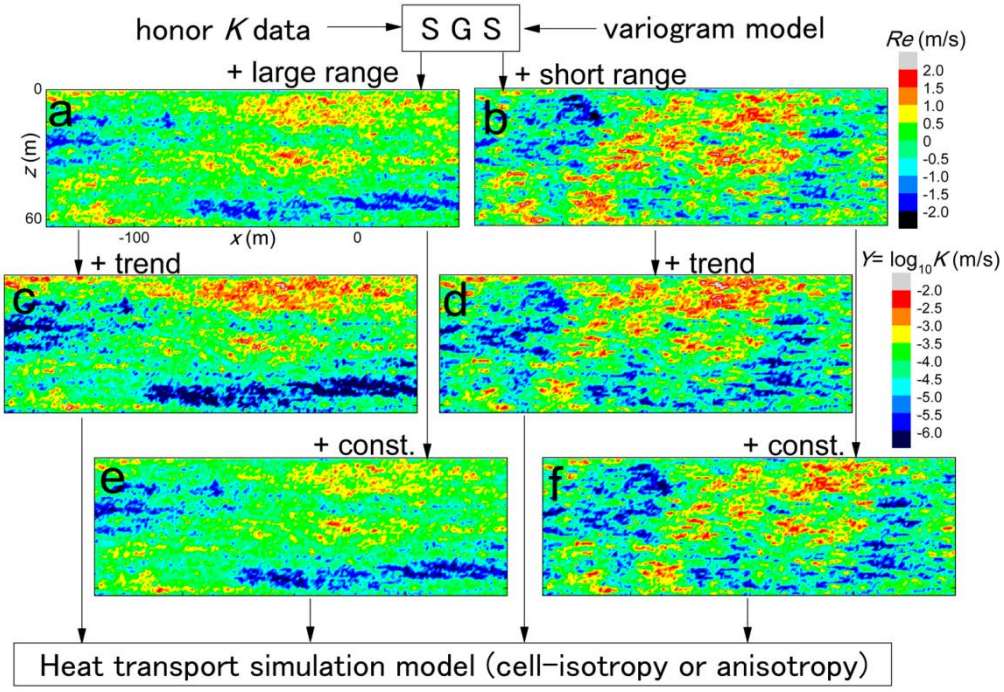

703

704 Figure 5 Conceptual flow chart showing the generating algorithm for the realization of the residuals

705 *R* using large (a) and small (b) ranges, and of the logarithm of hydraulic conductivity *Y* (c to f).

706

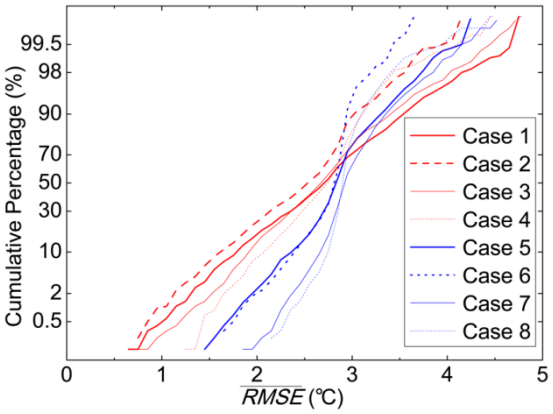

Figure 6 Cumulative percentage curves of $\overline{RMSE}$ for the eight simulation cases. Red lines indicate exponential decrease of *K* and blues lines have constant mean change; bold and thin lines represent large and small variogram ranges, respectively, and solid and dotted lines indicate cell isotropy and anisotropy, respectively.

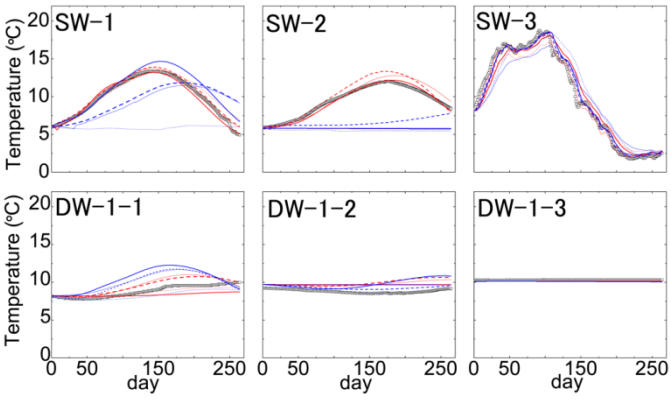

Figure 7 Calculated time series of groundwater temperature by extracted realizations of *Min* for the eight cases. Bold squares are observations, and color lines are the eight simulation cases denoted as in Fig. 6.

718 Table 1 Summary of $\overline{RMSE}$ in 1000 realizations of each study case.

Case	Conditions			Results			
	Trend	Range	Cell	*Me*	*Var*	*Min*	N_{RMSE}
1	*exponential decay*	*large*	*isotropy*	2.76	0.47	0.66	4
2			*anisotropy*	2.58	0.33	0.75	10
3		*small*	*isotropy*	2.73	0.35	0.62	2
4			*anisotropy*	2.79	0.19	1.27	*none*
5	*constant mean*	*large*	*isotropy*	2.89	0.15	1.43	*none*
6			*anisotropy*	2.87	0.07	1.59	*none*
7		*small*	*isotropy*	2.96	0.10	1.87	*none*
8			*anisotropy*	2.93	0.04	2.17	*none*

719